

RESEARCH ARTICLE

Rigid Motion Estimation using Accelerated Coordinate Descent (REACT) for MR Imaging

Kwang Eun Jang¹  | Dwight G. Nishimura² ¹Independent researcher, Republic of Korea²Magnetic Resonance Systems Research Lab (MRSRL), Department of Electrical Engineering, Stanford University, California, United States**Correspondence**

Kwang Eun Jang Email: kejang@gmail.com

Present Address

350 Jane Stanford Way, Stanford, CA 94305, USA

Funding Information

This work was partially supported by National Institutes of Health; Grant R01 HL127039

Purpose: To develop a computationally viable autofocus method for estimating 3D rigid motion in MR imaging.**Theory and Methods:** The proposed method, REACT, assumes a piecewise-constant motion trajectory and estimates the rigid motion parameters of individual temporal segments by optimizing an image-quality metric. Coordinate descent is adopted to decompose the high-dimensional optimization problem into a series of subproblems, each updating the motion parameters of a single temporal segment. The cost function of each subproblem is assumed to be approximately locally convex under suitable acquisition conditions. Each subproblem is then solved using a derivative-free solver, thereby avoiding an exhaustive grid search. Numerical simulations were conducted to investigate the local convexity assumption. REACT was evaluated for respiratory motion correction on *in vivo* free-breathing coronary MR angiography datasets acquired using a 3D cones trajectory with image-based navigators (iNAVs). An autofocus nonrigid motion correction method was also evaluated for comparison. Coronary artery sharpness was quantified using unbounded image edge profile acutance (u-IEPA).**Results:** In numerical simulations, the objective surfaces of the subproblems were approximately locally convex when the current motion estimate was close to the desired solution. In the *in vivo* study, REACT yielded higher u-IEPA than the conventional iNAV-based translational motion-estimation method for both the left anterior descending artery (LAD) and right coronary artery. REACT also yielded higher u-IEPA for the LAD than the autofocus nonrigid motion correction method.**Conclusion:** This study demonstrates the feasibility of coordinate descent for autofocus motion correction in MR imaging.**KEYWORDS:**

Motion Correction, Autofocus, Coordinate Descent, Free-breathing Coronary MRA

WORD COUNT: 4846

1 | INTRODUCTION

MR imaging is inherently motion-sensitive because any motion over multiple repetition times (TRs) introduces inconsistencies in the k -space data¹. To address motion, numerous methods have been proposed¹. This work falls within the category of autofocus methods², also known as autocorrection methods³. In these methods, motion is estimated by optimizing a metric that quantifies reconstructed image quality, because motion-induced inconsistencies in k -space data typically manifest as image degradations such as blurring and ghosting.

In the autofocus approach, the motion trajectory is commonly modeled as piecewise constant over time, reducing the motion-estimation problem to finding the motion parameters for each temporal segment. Early autofocus methods employed grid searches, often combined with scheduling heuristics such as coarse-to-fine and multiresolution approaches^{2,3,4}. Subsequently, an analytic derivative of an autofocus metric with respect to rigid motion parameters was derived to enable gradient-based optimization⁵. A data-consistency approach was also proposed, which jointly estimates the motion-free image and motion trajectory using a reduced forward model⁶. The autofocus approach was further extended to nonrigid motion correction by modeling nonrigid motion as localized translations^{7,8}.

One of the main challenges in the autofocus framework is to solve a high-dimensional optimization problem. Even when restricted to 3D rigid motion, the optimization problem involves $6N$ unknowns—three for translation and three for rotation—where N denotes the number of temporal segments.

In this work, we adopt the coordinate-descent approach^{9,10,11} for autofocus motion correction. The key idea of coordinate descent is to decompose a high-dimensional optimization problem into a series of tractable subproblems, each updating a single *coordinate* while keeping all others fixed. In our setup, each coordinate corresponds to the motion parameters of one temporal segment, and each subproblem therefore involves only six unknowns. A conceptual overview of the proposed framework is shown in Figure 1.

We hypothesize that image quality varies smoothly as the motion parameters of a *single* temporal segment are adjusted, such that the associated cost function is approximately locally convex, provided that the current motion estimate is sufficiently close to the desired solution. This local convexity likely arises because, as this small subset of motion parameters is perturbed, the *active* component (i.e., the Fourier transform of the corresponding k -space data) interferes constructively or destructively with the *static* background (i.e., the Fourier

transform of the remaining data), thereby altering the levels of blurring and ghosting. The objective functions of the coordinate-descent subproblems may therefore exhibit local convexity around the deviation that yields maximal coherence between the active component and the static background. This hypothesis not only supports the coordinate-descent approach for autofocus motion correction but also eliminates the need for exhaustive grid searches, since local convexity enables modern numerical solvers to efficiently solve the subproblems.

For our coordinate-descent approach, we impose a few conditions on data acquisition. We assume that the k -space data collected within each temporal segment (a) are sufficiently distributed across k -space and (b) have nontrivial energy in the image domain. The former enables motion estimation along all degrees of freedom, and the latter ensures that perturbing the motion parameters for any single temporal segment produces measurable changes in an autofocus metric. We also assume that the signal-to-noise ratio (SNR) is adequate. Segmented acquisitions that collect data over multiple acquisition windows can satisfy these conditions if the sampling trajectory within each window provides broad k -space coverage.

Coordinate-wise updates, however, can be inefficient when low-frequency discrepancies remain between the current estimates and the desired solution. In the context of motion estimation, this issue can arise when periodic motion induces correlated (low-frequency) errors across groups of temporal segments. In addition, without good initialization, the coordinate-descent approach may yield inaccurate motion estimates because the assumed local convexity of the coordinate-wise cost function may no longer hold.

To address these issues, we introduce Rigid motion Estimation using Accelerated Coordinate descenT (REACT), which incorporates Nesterov acceleration^{12,13} and a group-wise update. With Nesterov acceleration, 3D rigid motion is estimated by alternating between global and coordinate-wise updates: the motion parameters of all temporal segments are tentatively updated using the previous increments and then refined via coordinate-wise updates. The group-wise update is employed to more directly address low-frequency discrepancies and to reduce overall computation time by lowering the number of subproblems to be solved. We also present successive 1D sweeps and a learning-rate ramp-up to improve the robustness of REACT when good initial estimates are unavailable.

A Python implementation of REACT will be made publicly available on GitHub upon publication of this work.

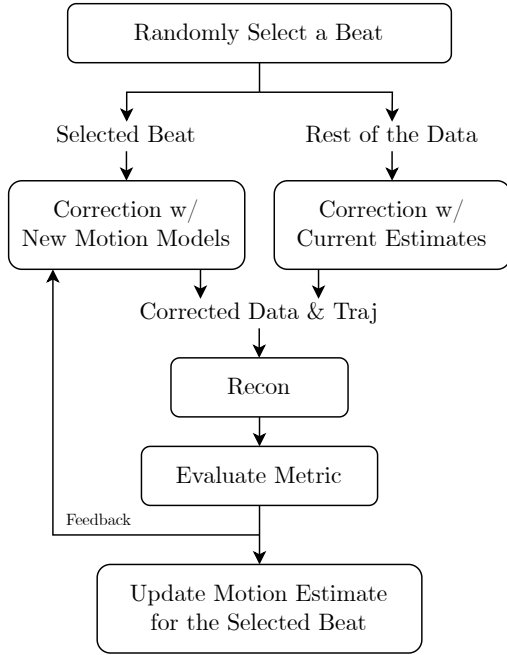


FIGURE 1 Conceptual overview of the proposed approach, where the motion parameters of one temporal segment are updated while all others are kept fixed. A “beat” refers to a temporal segment during which the object is assumed stationary.

2 | THEORY

Table 1 summarizes the notation used in this paper. Following prior work^{2,3,4,5}, the motion trajectory is assumed to be piecewise constant in time over the course of the segmented acquisition. In this paper, a “beat” refers to the smallest time interval during which the object is assumed to remain stationary (i.e., one temporal segment). In free-breathing coronary MR angiography, for example, the heart is typically assumed to remain stationary during the relatively short acquisition window of every heartbeat¹⁴.

2.1 | Rigid Motion Correction in k -space

We use rotation vectors (rotvecs) \mathbf{v} to represent 3D rotations. A rotvec is a 3D vector whose direction and magnitude indicate the rotation axis and rotation angle (in radians), respectively¹⁵. The corresponding rotation matrix $\mathbf{R}(\mathbf{v})$ is synthesized using Rodrigues’ formula¹⁵.

Rigid motion in image space can be represented in k -space through the properties of the Fourier transform¹⁶. Specifically, a translation in image space introduces a linear phase in k -space, while a rotation in image space results in a rotation of the sampling trajectory. Our goal is to estimate the translation vector \mathbf{t}_i and rotation

TABLE 1 Notation.

Symbol	Description	Size
N	Number of temporal segments	(1×1)
n	Iteration index	(1×1)
\square_i	Quantity at the i -th beat	N/A
$\square^{(n)}$	Quantity at iteration n	N/A
$\square^{(-1)}$	Uncorrected data or trajectory	N/A
t	Time	(1×1)
$\mathbf{k}(t)$	Sampling trajectory at t	(3×1)
$\mathbf{s}(t)$	Density-corrected k -space data at t	(1×1)
\mathbf{t}	Translation vector	(3×1)
\mathbf{v}	Rotation vector (rotvec)	(3×1)
\mathbf{x}	Rigid vector ($\mathbf{x}^T = [\mathbf{t}^T, \mathbf{v}^T]$)	(6×1)
\mathbf{X}	Stacked rigid vectors (i.e., $[\mathbf{x}_1, \dots, \mathbf{x}_N]$)	$(6 \times N)$
\oplus	Addition operator for rigid vectors	N/A
$\mathbf{R}(\mathbf{v})$	Rotation matrix induced by \mathbf{v}	(3×3)
$\mathbf{p}^{(n)}$	Increment of a rigid vector at iteration n	(6×1)
\mathbf{P}	Stacked increments of rigid vectors	$(6 \times N)$
$\hat{\mathbf{d}}$	Optimal deviation of a rigid vector	(6×1)
\mathbf{g}	Set of beat indices	N/A
\mathbf{G}	Stacked beat-index sets	N/A
$ \mathbf{g} $	Number of beat indices in \mathbf{g}	(1×1)
$ \mathbf{G} $	Number of beat-index sets in \mathbf{G}	(1×1)
$f(\mathbf{x}_i \mathbf{X})$	Cost function with respect to \mathbf{x}_i while the other rigid vectors are fixed.	N/A
$\alpha^{(n)}$	Learning rate at iteration n	(1×1)
$\beta^{(n)}$	Nesterov momentum at iteration n	(1×1)

vector \mathbf{v}_i for each beat i , such that the corresponding sampling trajectory and k -space data are corrected as

$$\mathbf{k}_i(t) = \mathbf{R}(\mathbf{v}_i) \cdot \mathbf{k}_i^{(-1)}(t), \quad (1)$$

$$\mathbf{s}_i(t) = \mathbf{s}_i^{(-1)}(t) \exp\left(j2\pi \left(\mathbf{t}_i^T \cdot \mathbf{k}_i^{(-1)}(t)\right)\right), \quad (2)$$

where $\mathbf{k}_i^{(-1)}(t)$ and $\mathbf{s}_i^{(-1)}(t)$ denote the uncorrected sampling trajectory and k -space data of the i -th beat, respectively.

2.2 | Image Gradient Entropy

We use image gradient entropy as the image-quality metric to be minimized, following the recommendation from the comparative study of McGee *et al.*³ on metrics for autocorrection approaches. Because the motion correction described by (1) and (2) is applied globally to the entire image, we introduce a binary mask \mathbf{W} to localize the metric to a region of interest (ROI), such as the heart. The image gradient entropy h used in this work

is computed as

$$h = - \sum_{\text{voxel}} \bar{\mathbf{H}} \log_2(\bar{\mathbf{H}}), \quad (3)$$

$$\bar{\mathbf{H}} = \frac{\mathbf{H}}{\sum_{\text{voxel}} \mathbf{H}}, \quad (4)$$

$$\mathbf{H} = \mathbf{W} \sqrt{|\nabla_x \mathbf{I}|^2 + |\nabla_y \mathbf{I}|^2 + |\nabla_z \mathbf{I}|^2}, \quad (5)$$

where \mathbf{I} is the reconstructed image, \mathbf{H} is the masked image gradient magnitude, and ∇_x , ∇_y , and ∇_z are finite-difference operators along the x , y , and z directions, respectively. Unlike the separable entropy used by Loktyushin et al.⁵, which is defined as the sum of the entropies of the individual gradient components, the metric in (3) is rotationally invariant.

2.3 | Coordinate Descent

Our task is to estimate the N sets of translation and rotation vectors— $6N$ unknowns in total—that minimize the image-quality metric defined in (3). For such high-dimensional optimization problems, coordinate-descent algorithms have been shown to be highly effective^{9,10,11,17,18}. The key features of the coordinate-descent approach are: (a) updating one *coordinate* at a time while keeping the others fixed, (b) immediately using the updated coordinate in subsequent updates, and (c) updating the coordinates in a randomized order to prevent systematic bias.

Algorithm 1 presents the pseudocode for a direct adaptation of coordinate descent to the motion-estimation problem. For each beat, a numerical solver estimates the optimal deviation from the current motion estimate, and this process is repeated across all temporal segments in a randomized order. Based on the hypothesis that each coordinate-wise subproblem has an approximately locally convex cost function, we employ a derivative-free solver to update the six motion parameters, avoiding exhaustive grid searches and gradient-based methods that require nontrivial analytic derivatives of the image-quality metric in (3) with respect to the motion parameters.

2.4 | Nesterov Acceleration

The Nesterov-accelerated gradient descent method^{12,13} is given as

$$x^* \leftarrow x^{(n)} + \beta^{(n)}(x^{(n)} - x^{(n-1)}), \quad (6)$$

$$x^{(n+1)} \leftarrow x^* - \alpha^{(n)} \nabla f(x^*), \quad (7)$$

where $\alpha^{(n)}$ and $\beta^{(n)}$ denote the learning rate and the Nesterov momentum at iteration n , respectively. In this scheme, the solution is temporarily updated using a

Algorithm 1 Direct Adaptation of Coordinate Descent

- 1: Initialize:
- 2: $\mathbf{X}^{(0)} \leftarrow (\mathbf{x}_1^{(0)}, \dots, \mathbf{x}_N^{(0)})$
- 3: **for** n **do**
- 4: $\mathbf{X}^{(n+1)} \leftarrow \mathbf{X}^{(n)}$
- 5: $\mathbf{g} \leftarrow \text{randomize } \{1, \dots, N\}$
- 6: **for** $i \in \mathbf{g}$ **do**
- 7: $\hat{\mathbf{d}}_i \leftarrow \text{argmin } f(\mathbf{d}_i \oplus \mathbf{x}_i^{(n)} \mid \mathbf{X}^{(n+1)})$
- 8: $\mathbf{x}_i^{(n+1)} \leftarrow \alpha^{(n)} \hat{\mathbf{d}}_i \oplus \mathbf{x}_i^{(n)}$
- 9: **end for**
- 10: **end for**

Line 7: Using $\mathbf{X}^{(n+1)}$ reflects immediate use of the updated coordinate.

fraction of the previous increment, and then a gradient descent step is performed from this intermediate point.

Algorithm 2 presents the pseudocode for the Nesterov-accelerated version of Algorithm 1. Here, we draw an analogy between the gradient descent step and the process of solving the subproblem for the optimal deviation. The key departure from Algorithm 1 is the alternation between a global update and a series of coordinate-wise updates. The motion estimates for all temporal segments are first temporarily updated, after which the motion of each beat is refined individually. This intermediate update involves only additions of translation and rotation vectors with their previous increments, without invoking the numerical solver. We use the FISTA-style Nesterov momentum sequence¹³, defined as

$$\beta^{(n)} = \frac{l^{(n)} - 1}{l^{(n+1)}}, \quad l^{(n+1)} = \frac{1 + \sqrt{1 + 4(l^{(n)})^2}}{2}, \quad l^{(0)} = 1. \quad (8)$$

2.5 | Group-wise Update

To better address low-frequency discrepancies between the current estimates and the desired solution, we incorporate a group-wise update strategy. This approach also reduces computational cost by decreasing the number of numerical solver calls. Algorithm 3 presents the pseudocode for the proposed REACT method. In each iteration, the temporal segments are classified into several groups such that beats within a group have similar motion-estimation errors. In the Nesterov acceleration step, the mean increment within each group is used. Subsequently, the optimal deviation is estimated for each group and applied to all beats in the group. As the iteration progresses, the number of elements in each group is reduced; when all groups have size one ($\mathbf{g}_j = \{j\}$), REACT becomes equivalent to Algorithm 2.

We assume a strong correlation between the *state* of the imaging object and the error in the current motion

Algorithm 2 Pseudocode for REACT w/o Grouping

```

1: Initialize:
2:  $\mathbf{X}^{(0)} \leftarrow (\mathbf{x}_1^{(0)}, \dots, \mathbf{x}_N^{(0)})$ 
3:  $\mathbf{P}^{(0)} \leftarrow (\mathbf{0}, \dots, \mathbf{0})$ 
4: for  $n$  do
5:    $\beta^{(n)} \leftarrow$  Nesterov momentum
6:   for  $i = (1, \dots, N)$  do
7:      $\mathbf{x}_i^* \leftarrow \beta^{(n)} \mathbf{p}_i^{(n)} \oplus \mathbf{x}_i^{(n)}$ 
8:   end for
9:    $\mathbf{X}^{(n+1)} \leftarrow \mathbf{X}^*$ 
10:   $\mathbf{g} \leftarrow$  randomize  $\{1, \dots, N\}$ 
11:  for  $i \in \mathbf{g}$  do
12:     $\hat{\mathbf{d}}_i \leftarrow \operatorname{argmin} f(\mathbf{d}_i \oplus \mathbf{x}_i^* | \mathbf{X}^{(n+1)})$ 
13:     $\mathbf{x}_i^{(n+1)} \leftarrow \alpha^{(n)} \hat{\mathbf{d}}_i \oplus \mathbf{x}_i^*$ 
14:     $\mathbf{p}_i^{(n+1)} \leftarrow \alpha^{(n)} \hat{\mathbf{d}}_i \oplus \beta^{(n)} \mathbf{p}_i^{(n)}$ 
15:  end for
16: end for

```

Line 7: Look-ahead (extrapolation) step for Nesterov acceleration.
Line 13: Sum of coordinate-wise update and look-ahead increment.

estimate. For example, respiratory motion across different heartbeats tends to be similar when those heartbeats occur at the same respiratory phase. Under this assumption, beats with similar motion-estimation errors can be identified by classifying the temporal segments into groups.

Various prior information and additional data can be utilized for grouping. Initial motion estimates may be a natural choice when available. When image-based navigators (iNAVs) are acquired, spatial features extracted from the iNAVs can serve as feature vectors for clustering. External physiological signals, such as respiratory traces, can also be incorporated.

2.6 | Optional 1D Sweeps and Learning-Rate Ramp-Up

When good initial estimates are unavailable, REACT may yield inaccurate estimates because the coordinate-wise cost function may no longer exhibit local convexity. To improve robustness in such scenarios, we optionally perform a coarse grid search on one temporal segment before each coordinate-wise optimization to provide an initial guess for translational motion. Instead of a full 3D search, we use three successive 1D sweeps, since the additional phase term due to translation can be factorized into separable components along each spatial direction. When motion exhibits a dominant direction—such as the superior–inferior (SI) direction in respiratory motion—this strategy can be improved by first sweeping along the dominant direction, followed by the remaining two directions.

Algorithm 3 Pseudocode for REACT w/ Grouping

```

1: Initialize:
2:  $\mathbf{X}^{(0)} \leftarrow (\mathbf{x}_1^{(0)}, \dots, \mathbf{x}_N^{(0)})$ 
3:  $\mathbf{P}^{(0)} \leftarrow (\mathbf{0}, \dots, \mathbf{0})$ 
4: for  $n$  do
5:    $\mathbf{G} \leftarrow$  randomize(group  $\{1, \dots, N\}$ )
6:    $\beta^{(n)} \leftarrow$  Nesterov momentum
7:   for  $\mathbf{g}_j \in \mathbf{G}$  do
8:      $\mathbf{p}_j^* \leftarrow \operatorname{mean}(\mathbf{P}^{(n)}[\mathbf{g}_j])$ 
9:     for  $i \in \mathbf{g}_j$  do
10:       $\mathbf{x}_i^* \leftarrow \beta^{(n)} \mathbf{p}_j^* \oplus \mathbf{x}_i^{(n)}$ 
11:    end for
12:  end for
13:   $\mathbf{X}^{(n+1)} \leftarrow \mathbf{X}^*$ 
14:  for  $\mathbf{g}_j \in \mathbf{G}$  do
15:     $\hat{\mathbf{d}}_j \leftarrow \operatorname{argmin} f(\mathbf{d}_j \oplus \mathbf{X}^*[\mathbf{g}_j] | \mathbf{X}^{(n+1)})$ 
16:    for  $i \in \mathbf{g}_j$  do
17:       $\mathbf{x}_i^{(n+1)} \leftarrow \alpha^{(n)} \hat{\mathbf{d}}_j \oplus \mathbf{x}_i^*$ 
18:       $\mathbf{p}_i^{(n+1)} \leftarrow \alpha^{(n)} \hat{\mathbf{d}}_j \oplus \beta^{(n)} \mathbf{p}_j^*$ 
19:    end for
20:  end for
21: end for

```

Line 8: \mathbf{p}_j^* is the mean increment within group \mathbf{g}_j .
Lines 14–16: The group update $\hat{\mathbf{d}}_j$ is applied to all beats in \mathbf{g}_j .

To further improve stability, we optionally use smaller learning rates $\alpha^{(n)}$ during early iterations. This is because conservative early updates help avoid overly aggressive motion corrections before a coherent background has formed (i.e., before the objective function becomes approximately locally convex). We use the following sinusoidal ramp-up schedule for $\alpha^{(n)}$ when needed:

$$\alpha^{(n)} = \begin{cases} \sin\left(\frac{\pi(n+1)}{2(N_{\text{ramp}}+1)}\right), & \text{if } n < N_{\text{ramp}}, \\ 1, & \text{otherwise.} \end{cases} \quad (9)$$

3 | METHOD

Numerical simulations using a 2D translational motion model were conducted to investigate whether the coordinate-descent subproblem cost function is locally convex. REACT was then evaluated on *in vivo* free-breathing, cardiac-gated coronary MR angiography datasets for respiratory motion correction.

3.1 | Numerical Simulations

A numerical brain phantom was generated by downsampling an *ex vivo* brain MR image¹⁹ from 100 μm to

TABLE 2 REACT Parameters.

Method	Motion	iNAVs	Nesterov	Group	Ramp	No. Iter.	Tol.	1D Sweeps	Search Range
Numerical Study	2D Tran	–	✓	–	3	3 (3.00)	0.01	1 (LR→AP)	±2
REACT	3D Rigid	✓	✓	✓	–	6 (1.56)	0.1	–	±2
REACT-Tran	3D Tran	✓	✓	✓	–	6 (1.57)	0.1	–	±2
REACT-NoAcc	3D Rigid	✓	–	–	–	2 (2.00)	0.1	–	±2
SN-REACT (Stage-1)	3D Tran	–	✓	–	3	3 (3.00)	0.1	2 (SI→AP→LR)	±5 (SI), ±2.5 (AP/LR)
SN-REACT (Stage-2)	3D Rigid	–	✓	✓	–	6 (1.53)	0.1	–	±2

No. Iter. lists the number of iterations; values in parentheses denote the corresponding normalized iteration count (interval size $|\mathbf{G}^{(n)}|/N$). *1D Sweeps* gives the spacing and order for the successive 1D sweeps (SI: superior–inferior, AP: anterior–posterior, LR: left–right directions). The units of *Tol.*, *1D Sweeps*, and *Search Range* are mm.

0.5 mm and zero-padding to 384×320 . Two 2D acquisition schemes were simulated: interleaved multi-shot echo-planar imaging (EPI) (24 shots; 16 k_y -lines/shot) and interleaved spiral imaging similar to that described by Kasper et al.²⁰ (field of view (FOV) 23 cm, resolution 0.5 mm, 30 interleaves, 20 ms readout, maximum gradient amplitude 31 mT/m, and slew rate 200 mT/m/ms).

An eight-channel receive array with linear sensitivities was simulated. Complex Gaussian noise was added to the k -space data to set the SNR of the sum-of-squares (SoS) reconstruction to 3, measured within an elliptical ROI enclosing the brain. Translational motion was drawn independently for each shot/interleaf from a zero-mean uniform distribution with a range of ± 2 mm along each direction.

The REACT parameters used in the numerical simulations are summarized in Table 2 (first row). The initial 2D translation estimates were set to zero (i.e., no additional navigator data were used). At each iteration, the cost function was sampled on a 64×64 grid spanning ± 5 mm in each direction around the ground truth, and the resulting cost maps were averaged over shots/interleaves. Because image gradient entropy in (3) is insensitive to global translation, the motion-corrected image may be shifted relative to the ground truth. To generate centered cost maps, the translation estimates were shifted to have zero mean before the cost maps were computed.

3.2 | *In Vivo* Data Acquisition

Ten *in vivo* datasets were acquired on a GE Signa 1.5 T scanner (GE Healthcare, Waukesha, WI) using an 8-channel cardiac array coil. Data were collected over 610 heartbeats (7–10 minutes total) while eight healthy volunteers (1F, 7M) breathed normally. The study was approved by the Institutional Review Board, and written informed consent was obtained from all subjects. Eight

datasets were acquired using leading sagittal and trailing coronal 2D iNAVs²¹ (resolution = 3.1 mm), and two datasets were acquired using trailing 3D iNAVs²² (resolution = 4.4 mm). A 3D cones phyllotaxis trajectory²³ was employed, acquiring 18 conic interleaves per heart-beat (temporal resolution = 98 ms). The prescribed FOV and spatial resolution were $28 \text{ cm} \times 28 \text{ cm} \times 14 \text{ cm}$ and $1.2 \text{ mm} \times 1.2 \text{ mm} \times 1.25 \text{ mm}$, respectively²³. An alternating repetition time balanced steady-state free precession (ATR-bSSFP) sequence²⁴ was used with the following parameters^{21,23}: TR = 5.4 ms, TE = 0.6 ms, FA = 70° , and BW = ± 125 kHz.

3.3 | Motion-Estimation Methods Compared

The following abbreviations are used for the motion-estimation methods compared in the *in vivo* study. NoCo denotes no motion correction and serves as the baseline. Tran represents conventional translational motion estimation using iNAVs. REACT indicates the proposed method, initialized with Tran estimates. SN-REACT refers to a self-navigated version of REACT, which relies solely on imaging data (i.e., without iNAVs). REACT-Tran assumes translational motion only, and REACT-NoAcc omits both Nesterov acceleration and the group-wise update.

For additional comparison, the autofocus nonrigid motion correction method proposed by Ingle et al.⁸ was also implemented. In this approach, a motion basis set is defined to generate a finite set of motion-corrected images^{7,8}. The final motion-corrected reconstruction is then assembled from this set by selecting, at each voxel location, the voxel value from the image with the lowest local image gradient entropy^{7,8}. As in the method of Ingle et al.⁸, the motion basis sets were constructed by scaling the estimated translational motion trajectories. NR-Tran and NR-REACT denote the nonrigid motion

corrections based on the estimated translational motion trajectories obtained from **Tran** and **REACT**, respectively.

3.4 | Implementation

The parameters used for the **REACT** variants are summarized in Table 2. **SN-REACT** was performed in two stages. In Stage 1, only translation was estimated using **REACT** with successive 1D sweeps and a sinusoidal learning rate. In Stage 2, translation and rotation were jointly estimated using the same parameters as **REACT**, without 1D sweeps or learning-rate ramp-up.

The Bound Optimization BY Quadratic Approximation (**BOBYQA**) algorithm²⁵, implemented in the **NLopt** package²⁶ (**LN_BOBYQA**), was used as the numerical solver. For *in vivo* experiments, the tolerance for **LN_BOBYQA** was set to 0.1 mm, using a conversion factor of 1° per 1 mm.

For grouping in **REACT**, principal component analysis (**PCA**) was applied to extract spatial features from translational motion-corrected **iNAVs**. For **SN-REACT**, the translational motion estimates from Stage 1 were used as feature vectors. Clustering was then performed using a recursive k-means algorithm. The number of beats per group was reduced from 32 to 1 by a factor of 2 over six iterations: $|\mathbf{g}_j^{(n)}| \leq (32, 16, 8, 4, 2, 1)$.

Convergence speed was compared using normalized iteration indices with interval size $|\mathbf{G}^{(n)}|/N$. Because the number of subproblems (groups) is closely related to the computational load of **REACT**, the normalized iteration index is approximately proportional to the overall computation time.

During **REACT**, an accelerated SoS method was used. The reconstruction for each coil was decomposed into a dynamic component—gridded from the subset of data being updated—and a static background reconstructed from the remaining data. This implementation significantly reduced the overall computation time by allowing the static background to be precomputed while gridding only a small portion of the data on the fly. The FOV for the SoS reconstruction was set to 54 cm × 36 cm × 30 cm with an isotropic spatial resolution of 1.2 mm. The oversampling factor for gridding was set to 1.15, resulting in a matrix size of 518 × 346 × 288.

For the final image reconstruction, the Split Bregman algorithm²⁷ with total variation (TV) regularization was applied, using coil sensitivity maps estimated by **ESPIRiT**²⁸.

Initial estimates of translational motion (**Tran**) were obtained by registering each **iNAV** to a reference frame. For datasets with 3D **iNAVs**, 3D translational registration implemented in **SimpleITK**^{29,30} was applied. For

datasets with 2D **iNAVs**, 2D affine registration was employed instead, since the imaged slice of the heart could vary between heartbeats. A cross-correlation-based subpixel registration method³¹ was used to provide an initial guess for the **SimpleITK** registrations.

For the autofocus nonrigid motion corrections⁸ (**NR-Tran** and **NR-REACT**), parameters similar to those used by Ingle et al.⁸ were employed. More specifically, evenly spaced scale factors from 0× to 2× were used⁸ to scale the estimated translational motion trajectories, with nine, nine, and five samples along the superior–inferior, anterior–posterior, and left–right directions, respectively⁸. An isotropic window of 32 voxels (3.84 cm) weighted by a Hann window^{7,8} was used to evaluate the local image gradient entropy. TV denoising was applied to the assembled SoS reconstruction using the Split Bregman algorithm²⁷. For **NR-REACT**, rotational motion was not incorporated into the motion basis set; instead, rotational motion correction was applied to each basis image according to (1).

All numerical experiments were performed on two workstations, each equipped with an **NVIDIA RTX 3090 GPU**: one with an **AMD Ryzen 9 9900X CPU** and the other with an **AMD Ryzen 9 5900X CPU**. Each workstation processed five *in vivo* datasets.

3.5 | Assessment

For a quantitative assessment of coronary artery sharpness, we adapt the image edge profile acutance (**IEPA**) metric³² as follows:

$$\text{u-IEPA} = \frac{\text{Mean}(\{g_j\})}{\text{Max}(\{\mathbf{r}_j\}) - \text{Min}(\{\mathbf{r}_j\})}, \quad (10)$$

$$g_j = \text{RMS} \left(\left\{ \frac{\mathbf{r}_j[i+1] - \mathbf{r}_j[i]}{\Delta} \right\} \right), \quad (11)$$

where \mathbf{r}_j denotes the j -th cross-sectional intensity profile of the coronary artery, and Δ denotes its spatial sampling interval. Here, “u” stands for “unbounded”; because u-IEPA is normalized by the spatial resolution, it is not bounded within (0, 1) as in the original IEPA. This modification removes the dependency on spatial resolution, facilitating fair comparisons across different setups.

A non-radiologist manually annotated the left anterior descending (**LAD**) and right coronary (**RCA**) arteries using the 3D curved multi-planar reformatting (**MPR**) tool in **Horos**³³. The centerline paths of the coronary arteries were then generated by in-house software based on the manual annotations. Cross-sectional planes orthogonal to the artery centerline were identified at 1.2 mm intervals along each *curved path*, and 60 radial profiles were extracted from each plane with a spatial

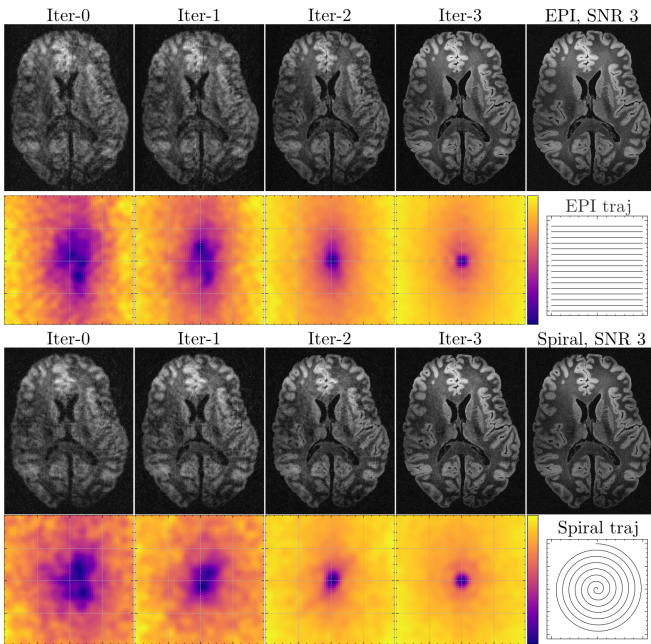


FIGURE 2 Numerical simulation (2D translation) with EPI (top) and spiral (bottom) acquisitions. Top row: motion-corrected reconstructions from iteration 0 (no correction) to iteration 3. Bottom row: objective values near the ground truth sampled within ± 5 mm. Rightmost: motion-free noisy reference (SNR=3) and an example EPI shot/spiral interleaf. As iterations progressed, the objective surface near the ground truth increasingly resembled a locally convex function.

sampling interval of 1.2 mm to measure u-IEPA scores. To obtain curved MPR images for visualization, the computationally refined curved paths were exported back to Horos.

4 | RESULTS

4.1 | Numerical Simulations

Figure 2 shows the motion-corrected reconstructions and the corresponding objective values near the ground truth at each REACT iteration. For both EPI and spiral acquisitions, REACT yielded accurate motion estimates after three iterations. As the REACT iterations progressed, the motion estimates became more accurate, and the objective surface near the ground truth increasingly resembled a locally convex function. These observations are consistent with our hypothesis that the cost function of each coordinate-descent subproblem is approximately locally convex when the current motion estimate is close to the desired solution and the SNR is adequate.

The average numbers of cost function evaluations per beat were 17.71 and 18.56 for the EPI and spiral acquisitions, respectively, which are substantially fewer than

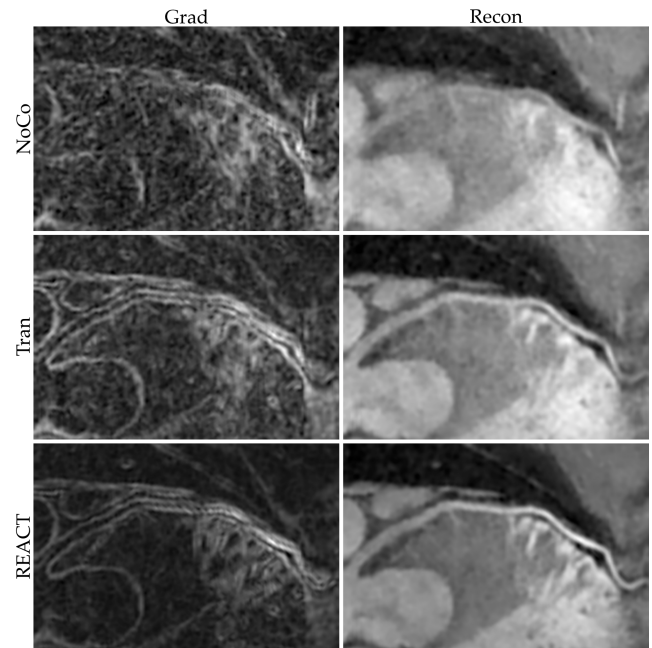


FIGURE 3 Curved MPR images along the LAD for NoCo (top), Tran (middle), and REACT (bottom). Left: image-gradient magnitudes (\mathbf{H} in (5)). Right: corresponding reconstructions. Compared with NoCo and Tran, REACT suppressed background graininess and produced sharper, more continuous vessel edges in the image-gradient magnitude map, resulting in improved vessel visibility in the reconstruction.

would be required for an exhaustive grid search. The elapsed times for three REACT iterations were 22.55 and 29.48 seconds for the EPI and spiral acquisitions, respectively.

4.2 | *In Vivo* Experiments

Figure 3 shows curved MPR images along the LAD and the corresponding image gradient magnitudes defined in (5). Compared with NoCo and Tran, REACT suppressed high-frequency background graininess and produced sharper, more continuous vessel edges in the image gradient magnitude map. These changes in the image gradient field translated into improved vessel sharpness and visibility in the motion-corrected reconstruction.

Figure 4 compares axial images across the different motion-estimation methods. REACT substantially improved vessel depiction over Tran. Although NR-Tran enhanced overall image sharpness relative to Tran—including non-cardiac structures such as the internal thoracic vessels (blue arrows)—its improvement in vessel sharpness was more limited, especially for the LAD (purple arrows). Compared to NR-Tran, REACT yielded higher vessel acutance, whereas NR-Tran provided superior sharpness in the myocardium and non-cardiac regions.

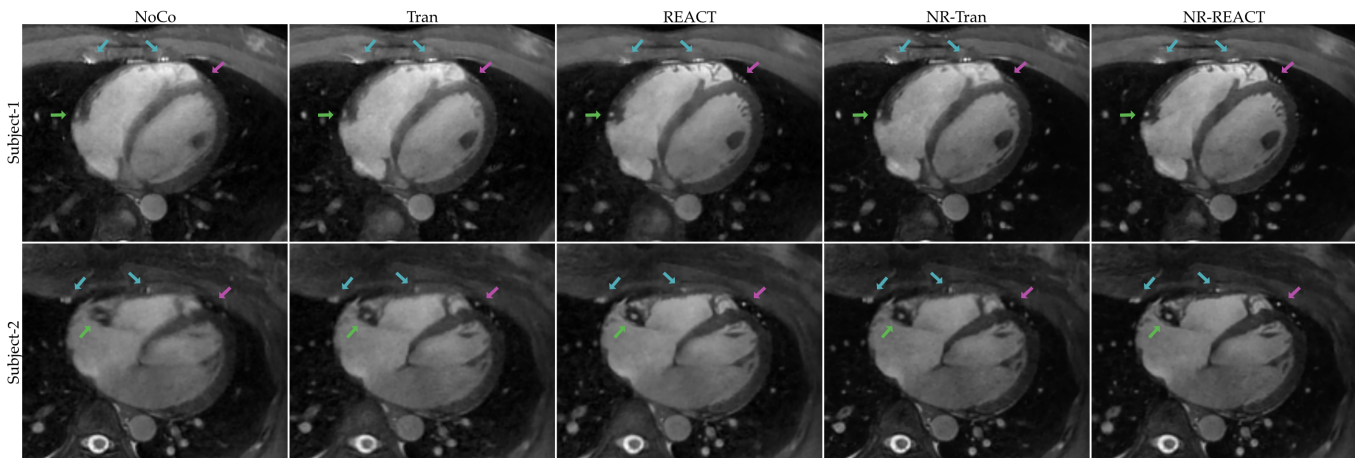


FIGURE 4 Axial images comparing NoCo, Tran, REACT, NR-Tran, and NR-REACT. Arrows highlight the LAD (purple), RCA (green), and internal thoracic vessels (blue). Compared with Tran, REACT substantially improved vessel depiction, whereas NR-Tran primarily enhanced overall sharpness with more limited gains in vessel delineation.

NR-REACT outperformed NR-Tran in both vessel visibility and overall image sharpness.

Since the motion correction used by Tran and REACT was performed in k -space, as described in (1) and (2), the non-cardiac regions appeared blurrier than in NoCo. Because the autofocus nonrigid motion corrections were computed in a voxel-wise manner, the non-cardiac regions appeared notably sharper than in their respective baselines. However, NR-Tran provided more limited improvement in vessel depiction relative to Tran than REACT did, largely because its correction capability was constrained by the motion basis set. Rotational motion and finer translational motion were not effectively captured by the motion basis set, because it was constructed by scaling the estimated translational motion trajectory using a relatively sparse set of scale factors.

Figure 5 illustrates the curved MPR images along the LAD and RCA. For the LAD, REACT showed enhanced vessel delineation compared to NR-Tran and substantially improved depiction over Tran. Although the autofocus nonrigid motion corrections (NR-Tran and NR-REACT) yielded higher vessel sharpness than their respective baselines (Tran and REACT), these incremental gains were relatively moderate. For the RCA, the differences between the motion-estimation methods were less pronounced than for the LAD, though the overall trend remained consistent.

Figure 6 compares curved MPR images along the LAD across the different REACT variants and Tran. The comparison between REACT-Tran and the other REACT methods indicates that correcting for rotational motion can considerably improve vessel acutance. SN-REACT outperformed Tran despite not utilizing iNAVs.

Figure 7(a) shows image-quality metrics plotted against normalized iteration indices for REACT and REACT-NoAcc. The LAD-1 datasets shown in Figure 5 was used for this analysis. Compared with REACT-NoAcc, REACT yielded lower image gradient entropy with fewer normalized iterations, resulting in improved image quality, as shown in the top row of Figure 6. This improvement can be largely attributed to the correction of low-frequency trends in the early iterations through group-wise updates. Although REACT consistently achieved lower image gradient entropy at convergence than REACT-NoAcc across other datasets, the corresponding improvements in vessel visibility were more modest, as illustrated in the bottom row of Figure 6.

Figure 7(b) shows scatter plots of translation magnitudes for three respiratory phases, with Tran on the x-axis and REACT on the y-axis. The respiratory phases were classified as end-expiration, mid-respiration, and end-inspiration using PCA features extracted from the iNAVs. In the end-inspiration phase, most points lie above the diagonal, indicating that REACT yielded larger translation estimates than Tran. The smaller translation estimates in Tran are likely due to mismatches between the end-expiration reference iNAV and the non-reference iNAVs. Because the heart can undergo rotations and nonrigid deformations across respiratory phases, iNAVs may not depict anatomy that differs only by translation; in our experiments, this mismatch appeared to result in conservative (i.e., smaller) translational shifts. Figure 7(b) also presents the distributions of rotation angles across respiratory phases. For most heartbeats, the estimated rotations were within $\pm 2^\circ$. Rotation angles tended to be slightly larger during the end-inspiration phase.

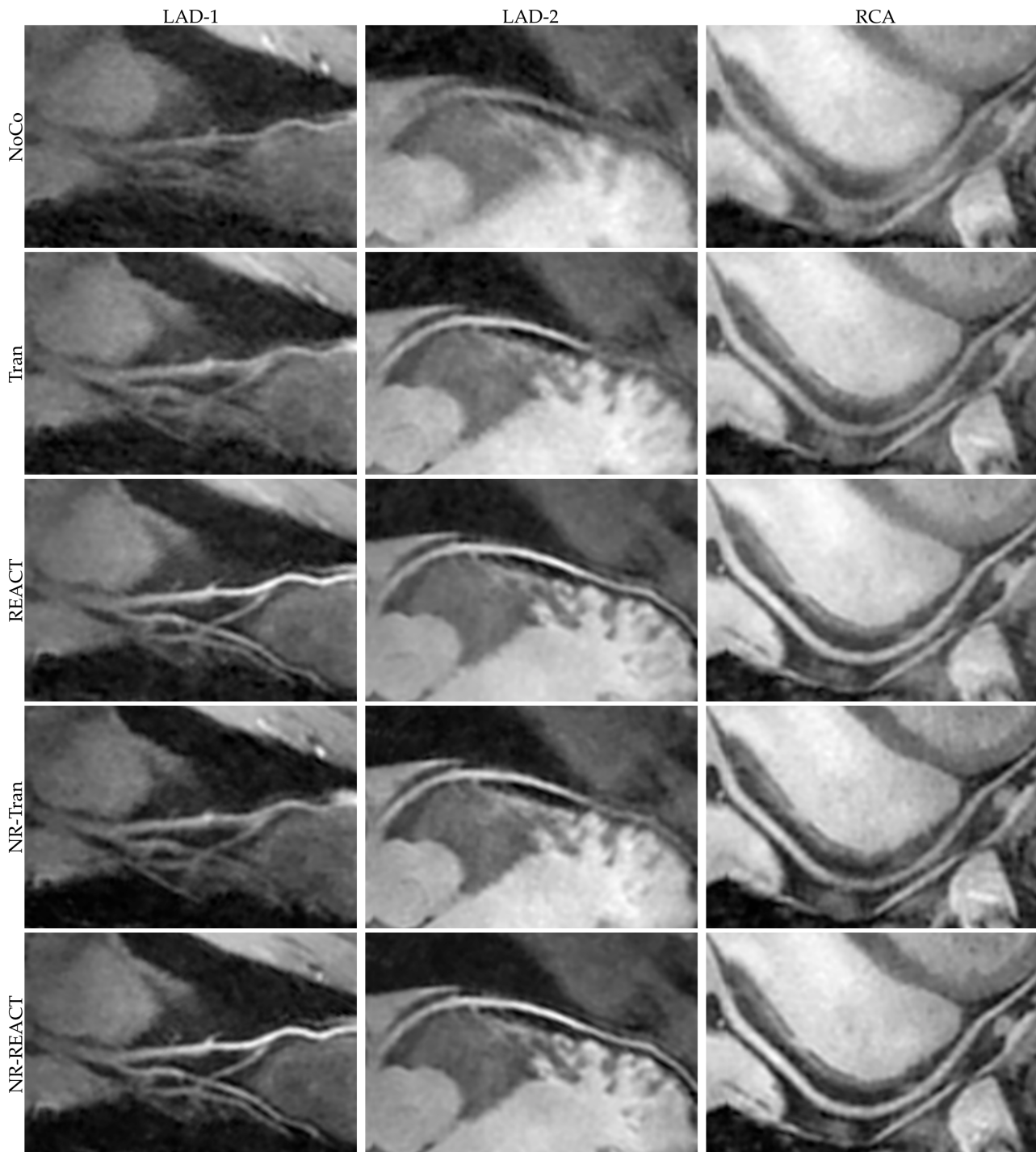


FIGURE 5 Curved MPR images along the LAD and RCA comparing NoCo, Tran, REACT, NR-Tran, and NR-REACT. REACT showed improved LAD delineation compared to Tran and NR-Tran, while autofocus nonrigid refinement (NR-Tran and NR-REACT) yielded moderate additional sharpening over their respective baselines. Similar, less pronounced differences were observed for the RCA.

Figure 7(c) summarizes u-IEPA scores relative to NoCo; selected two-sided paired t-tests are reported in Table 3.

REACT yielded higher u-IEPA for the LAD than Tran ($p < 10^{-4}$). Although u-IEPA scores for the RCA were generally lower than those for the LAD and inter-method

differences were smaller, REACT still provided higher u-IEPA than Tran ($p < 0.005$). SN-REACT also showed higher u-IEPA than Tran for both the LAD ($p < 0.005$) and RCA ($p < 0.01$).

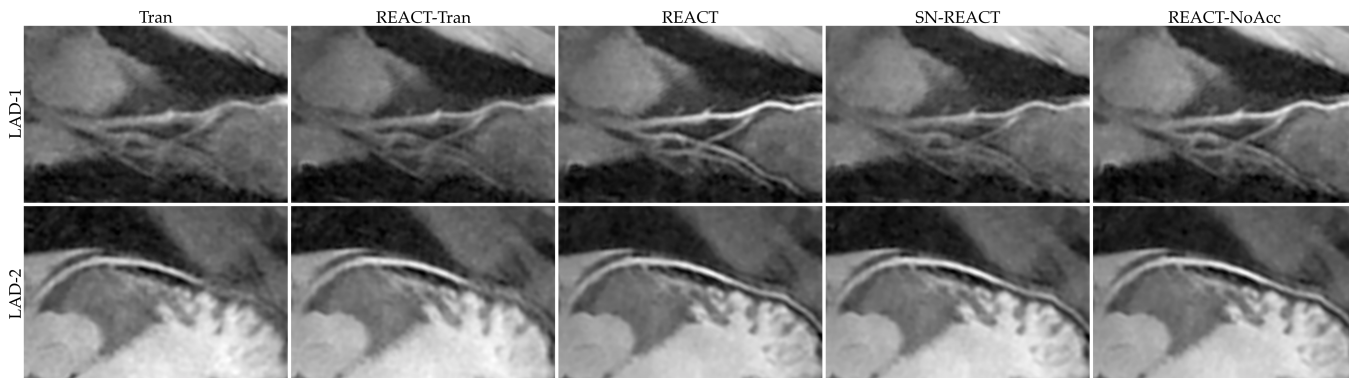
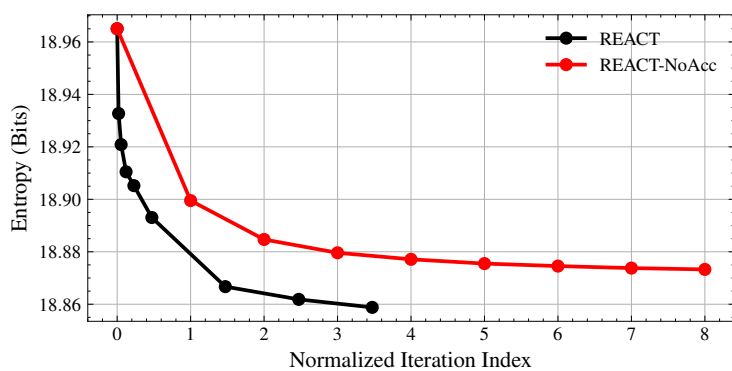
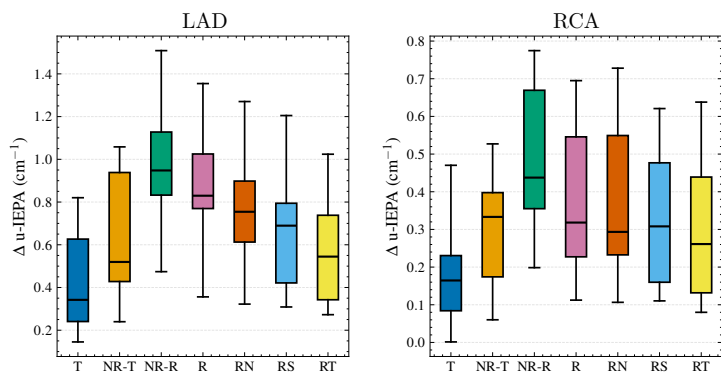


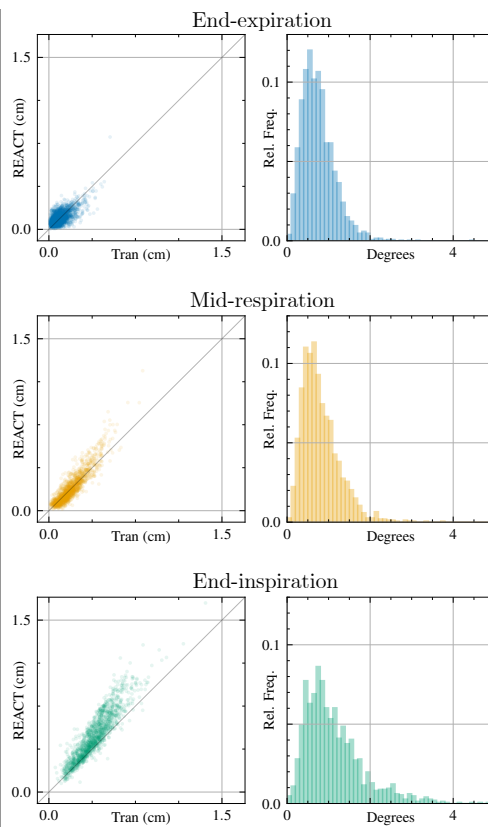
FIGURE 6 Curved MPR images along the LAD comparing Tran and REACT variants. Improvements due to rotational motion correction (REACT-Tran vs. other REACT variants) were observed. SN-REACT outperformed Tran without using iNAVs. Incorporating group-wise updates in early iterations resulted in improved motion correction (REACT-NoAcc vs. REACT, top row).



(a) Convergence Analysis



(c) Quantitative Analysis



(b) Motion Analysis

FIGURE 7 (a) **Convergence analysis:** image gradient entropy versus normalized iteration index; REACT achieves lower entropy with fewer normalized iterations than REACT-NoAcc. (b) **Motion analysis:** translation magnitudes estimated by Tran (x-axis) and REACT (y-axis) across respiratory phases (end-expiration, mid-respiration, and end-inspiration), with the identity line included for reference; rotation-angle distributions are also shown. In end-inspiration, most points lie above the diagonal, indicating larger translations estimated with REACT. (c) **Quantitative analysis:** boxplots of u-IEPA improvements relative to NoCo for the LAD and RCA. Abbreviations: T, Tran; NR-T, NR-Tran; NR-R, NR-REACT; R, REACT; RN, REACT-NoAcc; RS, SN-REACT; RT, REACT-Tran.

REACT-Tran resulted in higher u-IEPA than Tran for both the LAD ($p < 0.005$) and RCA ($p < 0.01$), indicating improved translational motion estimation over

the conventional iNAV-based method even without modeling rotation. REACT further achieved higher u-IEPA than REACT-Tran for both the LAD ($p < 0.001$) and

RCA ($p < 0.05$), supporting the benefit of incorporating rotational motion.

REACT showed higher u-IEPA than NR-Tran for the LAD ($p < 0.005$), consistent with the qualitative comparison. There was no significant difference in u-IEPA for the RCA ($p = 0.16$). NR-REACT demonstrated higher u-IEPA than NR-Tran for both the LAD ($p < 0.001$) and RCA ($p < 0.005$).

Although a relatively strict tolerance of 0.1 mm was set for the LN_BOBYQA solver over the search ranges of ± 2 mm and $\pm 2^\circ$, REACT required an average of 26.60 cost function evaluations per subproblem, far fewer than an exhaustive grid search would require. Six REACT iterations (equivalent to 1.56 normalized iterations) required 1.27 hours for REACT and 0.72 hours for REACT-Tran. Two iterations of REACT-NoAcc required 1.58 hours. The elapsed times for the first and second stages of SN-REACT were 2.31 and 1.14 hours, respectively.

5 | DISCUSSION

We have presented a new autofocus method, REACT, for estimating 3D rigid motion in MR imaging. REACT employs coordinate descent to decompose the high-dimensional optimization problem into a series of subproblems, each updating motion parameters for a single temporal segment while keeping the others fixed. Assuming the cost functions of these subproblems are approximately locally convex, each subproblem is efficiently solved using a derivative-free solver. We further incorporate Nesterov acceleration and group-wise updates to improve convergence and reduce overall computation time. When accurate initial motion estimates are unavailable, REACT can optionally perform successive 1D sweeps for initialization and apply a learning-rate ramp-up to improve robustness.

Our approach is computationally feasible, largely due to recent advances in derivative-free optimization methods such as the BOBYQA algorithm^{25,26}. In the *in vivo* experiments, only a few dozen cost function evaluations were required to solve each coordinate-descent subproblem, which is substantially fewer than would be required for an exhaustive grid search. Together with the numerical simulations, this finding is consistent with our hypothesis that the objective functions of the subproblems are approximately locally convex. Because of this local convexity, each subproblem can be solved efficiently using quadratic approximations of the cost function within the BOBYQA solver.

In principle, the proposed approach could incorporate analytic derivatives of the image-quality metric with respect to the motion parameters, as in the method

of Loktyushin et al.⁵. Although a gradient-based solver may reduce the number of cost function evaluations per subproblem, deriving and computing these derivatives can be nontrivial and computationally expensive for non-Cartesian acquisitions, where gridding usually relies on convolutional interpolation^{14,34}. Therefore, this study prioritized a derivative-free approach to ensure broader applicability and ease of implementation.

The correction of rotational motion is often neglected in free-breathing cardiac MRI reconstructions. This may be partly because, although rotational motion is more difficult to estimate from limited navigator data, translational motion correction often yields sufficiently good results. In our experiments, translational motion dominated the overall respiratory motion; however, incorporating rotational motion also provided noticeable improvements in image quality and vessel depiction. It may be beneficial to incorporate autofocus motion correction into the reconstruction pipeline to address rotational motion when additional computation time is available.

In this work, no regularization was applied for motion estimation because the motion between neighboring heartbeats often differs due to the relatively large temporal spacing between them. We did not observe any noticeable outlier motion estimates even without regularization. However, when the motion between neighboring temporal segments is smooth, it may be beneficial to include an additional term that penalizes large deviations among neighboring segments. In fact, the coordinate-descent methods for tomographic image reconstruction readily incorporated generalized Gaussian Markov random field (GGMRF) models for regularization^{10,17,18}, thanks to its pixel-wise update scheme.

To reduce the computational cost of objective function evaluations, we used the SoS reconstruction. In our implementation, only a small portion of the data was gridded on the fly while the static background was precomputed, which significantly accelerated the SoS reconstruction. However, the SoS method may suffer from aliasing artifacts when the data are highly undersampled. Future work could explore integrating more advanced reconstruction methods, such as deep learning-based techniques³⁵.

While SN-REACT demonstrated promising results without requiring initial motion estimates, the proposed approach can still benefit from initialization or other external information. Future work could explore motion-estimation methods that provide sufficiently accurate initial estimates while having minimal impact on data acquisition.

TABLE 3 Two-sided Paired t-tests for Selected Comparisons.

Comparisons (A \neq B)		u-IEPA (LAD)		u-IEPA (RCA)	
A	B	Diff	p-value	Diff	p-value
Tran	NoCo	0.425 \pm 0.251	4.6e-4	0.175 \pm 0.140	3.3e-3
NR-Tran	Tran	0.199 \pm 0.081	2.7e-5	0.127 \pm 0.079	6.7e-4
REACT	Tran	0.424 \pm 0.164	1.8e-5	0.194 \pm 0.140	1.8e-3
SN-REACT	Tran	0.250 \pm 0.166	1.0e-3	0.158 \pm 0.152	9.2e-3
REACT-Tran	Tran	0.141 \pm 0.109	2.8e-3	0.128 \pm 0.120	8.0e-3
REACT	REACT-Tran	0.283 \pm 0.168	4.8e-4	0.066 \pm 0.079	2.7e-2
REACT	NR-Tran	0.224 \pm 0.183	3.7e-3	0.067 \pm 0.140	1.6e-1
NR-REACT	NR-Tran	0.330 \pm 0.197	4.9e-4	0.180 \pm 0.140	2.8e-3

Values represent mean \pm standard deviation of metric differences (A - B).

6 | CONCLUSION

This study demonstrates the feasibility of the coordinate-descent approach for autofocus motion correction in MR imaging. The high-dimensional optimization problem is decomposed into a series of subproblems, each updating the motion parameters of a single temporal segment while keeping the others fixed. Our observations indicate that, provided the data acquisition satisfies certain conditions and the current motion estimate is sufficiently close to the desired solution, the cost functions of these subproblems exhibit approximate local convexity. Consequently, each coordinate-descent subproblem is solved efficiently using a derivative-free numerical solver, avoiding an exhaustive grid search. Experiments in free-breathing coronary MR angiography demonstrate that REACT accurately estimates rigid respiratory motion, yielding improved image quality and enhanced coronary artery depiction.

ACKNOWLEDGMENTS

The authors thank Dr. Mario O. Malavé for providing the *in vivo* datasets used in this study. This work was supported in part by NIH grant R01 HL127039. A preliminary version of this work was submitted in abstract form to the 2026 Annual Meeting of the ISMRM.

ORCID

Kwang Eun Jang  0009-0000-7031-1347

Dwight G. Nishimura  0009-0005-5963-765X

REFERENCES

- Zaitsev Maxim, Maclaren Julian, Herbst Michael. Motion artifacts in MRI: A complex problem with many partial solutions. *Journal of Magnetic Resonance Imaging*. 2015;42(4):887–901.
- Atkinson D., Hill D.L.G., Stoye P.N.R., Summers P.E., Keevil S.F.. Automatic correction of motion artifacts in magnetic resonance images using an entropy focus criterion. *IEEE Transactions on Medical Imaging*. 1997;16(6):903–910.
- McGee Kiaran P., Manduca Armando, Felmlee Joel P., Riederer Stephen J., Ehman Richard L.. Image metric-based correction (Autocorrection) of motion effects: Analysis of image metrics. *Journal of Magnetic Resonance Imaging*. 2000;11(2):174–181.
- Atkinson David, Hill Derek L.G., Stoye Peter N.R., et al. Automatic compensation of motion artifacts in MRI. *Magnetic Resonance in Medicine*. 1999;41(1):163–170.
- Loktyushin Alexander, Nickisch Hannes, Pohmann Rolf, Schölkopf Bernhard. Blind retrospective motion correction of MR images. *Magnetic Resonance in Medicine*. 2013;70(6):1608–1618.
- Haskell Melissa W., Cauley Stephen F., Wald Lawrence L.. TArgeted Motion Estimation and Reduction (TAMER): Data Consistency Based Motion Mitigation for MRI Using a Reduced Model Joint Optimization. *IEEE Transactions on Medical Imaging*. 2018;37(5):1253–1265.
- Cheng Joseph Y., Alley Marcus T., Cunningham Charles H., Vasanawala Shreyas S., Pauly John M., Lustig Michael. Non-rigid motion correction in 3D using autofocusing with localized linear translations. *Magnetic Resonance in Medicine*. 2012;68(6):1785–1797.
- Ingle R. Reeve, Wu Holden H., Addy Nii Okai, et al. Non-rigid autofocus motion correction for coronary MR angiography with a 3D cones trajectory. *Magnetic Resonance in Medicine*. 2014;72(2):347–361.
- Sauer K., Bouman C.. A local update strategy for iterative reconstruction from projections. *IEEE Transactions on Signal Processing*. 1993;41(2):534–548.
- Bouman C.A., Sauer K.. A unified approach to statistical tomography using coordinate descent optimization. *IEEE Transactions on Image Processing*. 1996;5(3):480–492.

11. Wright SJ. Coordinate descent algorithms. *Math Program.* 2015;151(1):3–34.
12. Nesterov Yurii. A method for solving the convex programming problem with convergence rate $O(1/k^2)$. *Dokl akad nauk Sssr.* 1983;269:543.
13. Beck Amir, Teboulle Marc. A Fast Iterative Shrinkage-Thresholding Algorithm for Linear Inverse Problems. *SIAM Journal on Imaging Sciences.* 2009;2(1):183–202.
14. Bernstein Matt A, King Kevin F, Zhou Xiaohong Joe. *Handbook of MRI pulse sequences.* Elsevier; 2004.
15. Lynch Kevin M, Park Frank C. *Modern Robotics.* Cambridge University Press; 2017.
16. Bracewell Ronald. *Fourier Analysis and Imaging.* Springer Science & Business Media; 2012.
17. Ye JC, Webb KJ, Bouman CA, Millane RP. Optical diffusion tomography by iterative-coordinate-descent optimization in a Bayesian framework. *Journal of the Optical Society of America A.* 1999;16(10):2400–2412.
18. Yu Zhou, Thibault Jean-Baptiste, Bouman Charles A., Sauer Ken D., Hsieh Jiang. Fast Model-Based X-Ray CT Reconstruction Using Spatially Nonhomogeneous ICD Optimization. *IEEE Transactions on Image Processing.* 2011;20(1):161–175.
19. Edlow Brian L., Mareyam Azma, Horn Andreas, et al. 7 Tesla MRI of the ex vivo human brain at 100 micron resolution. *Scientific Data.* 2019;6(1):244.
20. Kasper Lars, Engel Maria, Barmet Christoph, et al. Rapid anatomical brain imaging using spiral acquisition and an expanded signal model. *NeuroImage.* 2018;168:88–100.
21. Wu Holden H, Gurney Paul T, Hu Bob S, Nishimura Dwight G, McConnell Michael V. Free-breathing multiphase whole-heart coronary MR angiography using image-based navigators and three-dimensional cones imaging. *Magnetic Resonance in Medicine.* 2013;69(4):1083–1093.
22. Addy Nii Okai, Ingle R Reeve, Luo Jieying, et al. 3D image-based navigators for coronary MR angiography. *Magnetic Resonance in Medicine.* 2017;77(5):1874–1883.
23. Malavé Mario O., Baron Corey A., Addy Nii Okai, et al. Whole-heart coronary MR angiography using a 3D cones phyllotaxis trajectory. *Magnetic Resonance in Medicine.* 2019;81(2):1092–1103.
24. Leupold Jochen, Hennig Jürgen, Scheffler Klaus. Alternating repetition time balanced steady state free precession. *Magnetic Resonance in Medicine.* 2006;55(3):557–565.
25. Powell M. J. D.. *The BOBYQA algorithm for bound constrained optimization without derivatives.* Technical Report NA2009/06: University of Cambridge; 2009.
26. Johnson Steven G.. The NLOpt nonlinear-optimization package <http://github.com/stevengj/nlopt> Version 2.10.0; 2025.
27. Goldstein Tom, Osher Stanley. The Split Bregman Method for L1-Regularized Problems. *SIAM Journal on Imaging Sciences.* 2009;2(2):323–343.
28. Uecker Martin, Lai Peng, Murphy Mark J., et al. ESPIRiT—an eigenvalue approach to autocalibrating parallel MRI: Where SENSE meets GRAPPA. *Magnetic Resonance in Medicine.* 2014;71(3):990–1001.
29. Lowekamp Bradley Christopher, Chen David T, Ibáñez Luis, Blezek Daniel. The design of SimpleITK. *Frontiers in Neuroinformatics.* 2013;7:45.
30. McCormick Matthew Michael, Liu Xiaoxiao, Ibanez Luis, Jomier Julien, Marion Charles. ITK: enabling reproducible research and open science. *Frontiers in Neuroinformatics.* 2014;8:13.
31. Guizar-Sicairos Manuel, Thurman Samuel T., Fienup James R.. Efficient subpixel image registration algorithms. *Optics Letters.* 2008;33(2):156–158.
32. Biassioli Luca, Lindsay Alistair C., Choudhury Robin P., Robson Matthew D.. Loss of fine structure and edge sharpness in fast-spin-echo carotid wall imaging: Measurements and comparison with multiple-spin-echo in normal and atherosclerotic subjects. *Journal of Magnetic Resonance Imaging.* 2011;33(5):1136–1143.
33. Horos Project . Horos: Free and open-source medical image viewer <https://horosproject.org> Version 4.0.1; 2023.
34. Beatty Philip J., Nishimura Dwight G., Pauly John M.. Rapid gridding reconstruction with a minimal oversampling ratio. *IEEE Transactions on Medical Imaging.* 2005;24(6):799–808.
35. Heckel Reinhard, Jacob Mathews, Chaudhari Akshay, Perlman Or, Shimron Efrat. Deep learning for accelerated and robust MRI reconstruction. *Magnetic Resonance Materials in Physics, Biology and Medicine.* 2024;37(3):335–368.

How to cite this article: Jang KE and Nishimura DG (2026), Rigid Motion Estimation using Accelerated Iterative Coordinate Descent (REACT) for MR Imaging, *Magn. Reson. Med.*, 2026;00:1–6.